# The challenge of bias free coil combination for quantitative susceptibility mapping at ultra-high field

Steffen Bollmann[1], Simon Daniel Robinson[2], Kieran O'Brien[1,3], Viktor Vegh[1], Andrew Janke[1], Lars Marstaller[1], David Reutens[1], Markus Barth[1]

*[1]Centre for Advanced Imaging, The University of Queensland, Brisbane, Queensland, Australia.*
*[2]High Field Magnetic Resonance Centre, Department of Biomedical Imaging and Image-Guided Therapy, Medical University of Vienna, Austria.*
*[3]Siemens Healthcare Pty Ltd, Brisbane, Queensland, Australia.*

**Correspondence to:**
Steffen Bollmann
The University of Queensland
Centre for Advanced Imaging
Building 57, Research Road, St. Lucia
Brisbane, QLD, 4072
Australia
email: steffen.bollmann@cai.uq.edu.au

**Acknowledgements:** The authors thank Don Maillet, Rients Lootsma and Alan Hockings for their engineering and IT support. We thank Aiman Al-Najjar and Nicole Atcheson for acquiring the data and the participants involved in this study. The data acquisition was funded by the Australian Research Council Special Research Initiative: Science of Learning Research Centre (project number SR120300015). MB acknowledges funding from Australian Research Council Future Fellowship grant FT140100865, and VV and DR from Discovery grant DP140103593. SB acknowledges funding from UQ Postdoctoral Research Fellowship grant and an NVIDIA Hardware Seed Grant. The authors acknowledge the facilities of the National Imaging Facility (NIF) at the Centre for Advanced Imaging, The University of Queensland. We also want to thank the anonymous reviewers for their time and help in improving the manuscript.

**Ethical approval:**
All procedures performed in studies involving human participants were in accordance with the ethical standards of the institutional and/or national research committee and with the 1964 Helsinki declaration and its later amendments or comparable ethical standards.

**Word count:**
The body contains 3318/5000 words, 9/10 figures, 0 tables.

**Abbreviations used:**

| | |
|---|---|
| 3D | three-dimensional |
| 2D | two-dimensional |
| EPI | echo-planar-imaging |
| GRE | spoiled gradient echo |
| MRI | magnetic resonance imaging |
| SNR | signal-to-noise ratio |
| QSM | quantitative susceptibility mapping |
| GRAPPA | generalized auto-calibrating partially parallel acquisitions |
| TE | echo time |
| TR | repetition time |
| FOV | field of view |
| TGV | total generalized variation |
| FSL | FMRIB Software Library |
| BET | Brain Extraction Tool |
| PETRA | pointwise encoding time reduction with radial acquisition |
| COMPOSER | COMbining Phase data using a Short Echo-time Reference scan |

# Abstract (max. 200 words)

Purpose: Quantitative susceptibility mapping is a technique to estimate the magnetic property of tissue with particularly high sensitivity at ultra-high field. However, a key challenge at ultra-high field is the combination of phase data acquired using phased array receive coils. Several methods for combining phase data have been proposed, but the influence of coil combination choices on susceptibility quantitation has not been studied systematically.

Methods: We combined phase data using COMPOSER (COMbining Phase data using a Short Echo-time Reference scan) and a reference-free channel-by-channel method. We investigated the effect of the chosen combination method on susceptibility results in a group of 28 participants at 7 T.

Results: Our results show that reference scans can bias susceptibility values. Although the proposed reference-free channel-by-channel method cannot remove transmit field phase, it shows comparable results to the COMPOSER method where a high-resolution ultra-short echo-time reference scan was employed.

Conclusion: We conclude that ultra-short echo-time reference scans reduce quantitation bias and remove the transmit field phase when using COMPOSER to combine phase data and, not combining the phase data prior to susceptibility processing avoids this bias resulting in comparable results.



**Key words:**
COMPOSER, 3D-EPI, Ultra-high field, QSM, PETRA, atlas based segmentation

# Introduction

Magnetic susceptibility describes the magnetization of a sample when placed in an external magnetic field. The quantification of magnetic susceptibility based on MRI phase measurements has gained a lot of interest because it may yield quantitative information on myelin composition and iron, copper, and calcium content (1–4) in the brain. Quantitative susceptibility mapping (QSM) provides a unique gray/white matter contrast (5) and has the potential to deliver novel insights into tissue composition in health and disease (6,7). As calcium has a lower magnetic susceptibility than water, QSM can be used to visualize micro-bleeds (8) and differentiate them from microcalcifications (9). Additionally, it can be used to measure iron stores (7) in normal aging (10,11), Huntington's Disease (12), multiple sclerosis (6,13,14), Alzheimers's Disease (15) and Parkinson's Disease (16,17). The novel contrast generated using QSM may also enhance image guided planning of electrode placement in deep brain stimulation (18).

Quantitative and qualitative magnetic susceptibility MRI profit from the use of ultra-high field scanners, where improvements in glioma treatment response assessment (19), microbleed detection (20), and multiple sclerosis lesion characterization (21) have been demonstrated compared to lower field strength results. A problem at ultra-high field, however, is the optimal channel combination of phase data in the absence of a volume reference coil with which to correct for spatially dependent phase offsets. With the term phase offset we summarize the difference in phase between two channels which consists of a constant and a spatially dependent term: There is a common offset for every channel caused by $B1^+$ phase, eddy currents, gradient delay effects, and a phase offset that is different for every channel, caused by cable length and receive sensitivity $B1^-$ (22–24). At lower field strengths these offsets can be corrected for using a homogeneous volume reference coil measurement, i.e. a body transmit coil, but this technology is currently not available at 7 T. Transceive coils with inhomogeneous transmit and receive profiles are available for some MRI systems and allow the correction of phase offsets. However, transceive elements are not available in some custom coils, and therefore, we investigated ways which do not rely on transceive coils to correctly combine phase data.

Other methods for combining phase data have been proposed and are widely used, but the problem is that none of them is ideal for single-echo applications and quantitating susceptibility at ultra-high field: The simplest method, homodyne filtering (25–27), will result in a loss of low spatial frequency features thereby affecting quantitation in susceptibility mapping. Phase matching methods (28–31) fail in large objects and contain undefined contributions to the phase (23), which also makes these methods sub-optimal for accurate QSM. Other methods are based on phase difference between

echoes (32–36) or temporal phase evolution (37) and require multi-echo data, which is not always available. Methods, such as SENSE (38), could optimally combine data from multiple coils using a single echo, but without a homogenous volume reference coil, the required coil sensitivity maps cannot be generated easily.

A recent solution to the phase combination problem - COMbining Phase data using a Short Echo-time Reference scan (COMPOSER) – can approximate phase offsets by employing a phase reference scan at a very short echo time (39). The phase offset for each channel can then be subtracted from every channel before complex valued channel data can be summed to form a single image. Notably, it is important to use a short echo-time relative to T2* of the tissue of interest to limit the reduction in phase contrast and quantitation bias as well. Furthermore, the reference image should be artifact free as to not introduce noise and errors during the subtraction process.

We may assume that each channel has a sufficiently large field-of-view and high signal-to-noise ratio which allows estimation of the background field and computation of the QSM inverse problem. In such a case, it is possible to obtain the QSM result by processing each channel separately. The result is a channel-by-channel averaged susceptibility map wherein spatially dependent phase offsets caused by $B1^+$ phase, eddy currents, gradient delay effects and channel dependent phase offsets caused by cable length and receive sensitivity $B1^-$ are suppressed during background field correction. We refer to this method as the single channel (SC) method throughout the manuscript. This method has been shown to yield susceptibility maps without artifacts (40), but it has not yet been compared quantitatively to a reference scan approach.

We describe the effect of using different reference scans in the COMPOSER method and compare it to the SC method. Our goal is to provide an informed way of choosing an appropriate coil combination technique for 7 T QSM applications. Ideally, the chosen coil combination technique can efficiently be used with single-echo data without making limiting assumptions and produce as little quantitation bias as possible. Additionally, the coil combination technique should be robust to motion with little scan time overheads.

# Methods

We obtained written informed consent from participants prior to in vivo scanning as approved by the local human ethics committee. Multiple channel phase combination was investigated for 28 participants (21-34 years of age, 26.5 years on average, 14 males) on a 7 T whole-body research scanner (Siemens Healthcare, Erlangen, Germany), with maximum gradient strength of 70 mT/m and a slew rate of 200 mT/m/s. A 7 T Tx/32 channel Rx head array (Nova Medical, Wilmington, MA, USA)

was used for radio frequency transmission and signal reception. Third order shimming was employed to improve the B0-field homogeneity.

Data acquisition

To be able to assess the different phase combination methods, we acquired multiple echo time gradient recalled echo (GRE) 3D whole brain datasets: TR = 25 ms, TE = 4.4, 7.25, 10.2, 13.25, 16.4, 19.65, 23 ms (echo times were set based on a previously described approach (41)), flip angle = 13°, FOV = 210x181.5x120 $mm^3$, matrix = 280x242x160 (0.75 mm isotropic voxels), parallel imaging (GRAPPA, acceleration factor = 2, 24 auto-calibration lines), monopolar readout gradient, symmetric echo, 1116 Hz/Pixel, first echo flow compensated, TA = 7.9 min.

For the reference scan, we acquired a low spatial resolution 3D GRE with 3 echoes to achieve a short first echo time: TR = 8 ms, TE = 1.02, 3.06, 6.12 ms, flip angle = 5°, FOV = 245x245x182 $mm^3$, matrix = 70x70x52 (3.5 mm isotropic voxels), monopolar readout gradient, symmetric echo, 1211 Hz/Pixel, TA = 24 s.

We also acquired data using the prototype PETRA ultra-short-TE sequence (42) for use as a reference scan: TR = 1.99 ms, TE = 0.07 ms, flip angle = 2°, FOV = 288x288x288 $mm^3$, matrix = 288x288x288 (1 mm isotropic voxels), 847 Hz/Pixel, and TA = 2 min.

In one additional participant (male, 44 years of age) we acquired a 3D EPI dataset to investigate the application of COMPOSER and SC to 3D EPI data: TR = 73 ms, volume TR = 9.3 s, TE = 29 ms, flip angle 16°, FOV = 220x220x128 $mm^3$ (1 mm isotropic resolution), 1082 Hz/Pixel, TA = 11s. For this dataset we acquired a low resolution reference GRE-MRI scan with 3 echoes: TR = 7.9 ms, TE = 1.3, 3.5, 5.68 ms, flip angle = 5°, FOV = 245x245x210 $mm^3$, matrix = 70x70x60 (3.5 mm isotropic voxels), monopolar readout gradient, symmetric echo, 600 Hz/Pixel, TA = 27s.

Coil combination approaches

The high resolution GRE-MRI dataset was processed using COMPOSER and the SC approach (Figure 1). For COMPOSER we used 2 of the 3 echoes of the additionally acquired low-resolution GRE data (TE = 1.02 ms (lrGRE1) and TE = 3.06 ms (lrGRE2)) and the first echo of the ultra-short-TE PETRA data (TE = 0.07 ms). The registration between reference scans and the high-resolution scan was performed using FSL flirt (43,44). Then the individual channels of the reference scan were subtracted from the main scan and complex values were summed. For the single channel approach, we processed each channel separately without combining the phase data and as a last step the final susceptibility maps were calculated by computing the mean across all channels (40).


*Figure 1 – Outline of the processing steps. Single channel GRE data (blue arrows) are either processed directly using the single channel method or processed through COMPOSER, where reference scans (orange arrows) are used to combine the phase data. The combined phase (green arrows) is then processed with TGV. Then a mean is computed either across channels and echoes or across echoes leading to the final susceptibility maps.*

The 3D EPI dataset was combined using the first echo of the low resolution GRE-MRI data (TE = 1.3 ms) and the SC method.

Quantitative susceptibility mapping

All susceptibility processing was performed using a total generalized variation (TGV) based QSM algorithm (45) that incorporates phase unwrapping, background field removal and dipole inversion in a single step. The alpha parameter factor of TGV was set to 1, leading to second order TGV regularization terms with $alpha_0$ = 0.0015 and $alpha_1$ = 0.0005. The first-order primal-dual algorithm was run with a maximum of 1000 iterations. The echo times used for computing the tissue fields were all corrected for the echo time shift introduced by COMPOSER by subtracting the echo time of the reference scan from the echo time of the combined scan.

For each brain a mask was generated based on the first echo combined high resolution GRE-MRI magnitude image using the Oxford FMRIB Software Library (FSL) Brain Extraction Tool (BET2) (46) with a fractional intensity threshold of 0.3. The mask was used in all pipelines.

Evaluation

For evaluating the effects of the different coil combination methods we computed the phase data and susceptibility maps, corrected for the COMPOSER echo time shift as described above. Then, images from individual echo times were averaged and results were subtracted from each other to qualitatively interpret differences between combination methods.

We used an atlas based segmentation of sub-cortical structures such as the red nucleus, caudate, pallidum and putamen, upon which our coil combination investigation using QSM results was based. The *volgenmodel* pipeline (47–49) was used to construct a minimum deformation model. First, a weighted sum of the GRE-MRI magnitude images was computed, where every echo image was weighted by the ratio of echo time to the sum of all echo times to enhance the contrast of structures with high susceptibility. The weighted means were intensity normalized between 0 and 100 and histograms were clamped between 5 and 70 to visually increase contrast. First, the initial model was generated based on one individual dataset blurred using a kernel size of 4 mm to remove individual features. Then all original input images were aligned via a 12 parameter affine transformation and a normalized cross correlation objective function. The original input datasets were then resampled to the model space and transformed using a concatenation of the inverse transformation from model to participant space and the average transform. Finally, the next model stage was computed by using a robust averaging process of the resampled data, i.e., only including data within two standard

deviations of the mean. After the affine transformation, non-linear registration was used with incrementally decreasing step and smoothing kernel sizes. The final transformations from participant to atlas space were then applied to the QSM data and averaged across participants to generate the QSM model, as shown in Figure 2. Specific brain regions in the generated QSM model were segmented manually using ITK-SNAP (50), and regions segmented were transformed to participant space. Segmentations were read in Matlab (The Mathworks, Natick, MA, USA) and susceptibility values were extracted from the QSM datasets in participant space. The *volgenmodel* code is available on GitHub (https://github.com/CAIsr/volgenmodel, revision 33db3f3 was used for this manuscript) and the GRE-MRI and QSM models can be viewed in an online 3D viewer, *tissuestack*, (http://www.tissuestack.org) and can also be downloaded (http://www.imaging.org.au/Human7T/QSM).

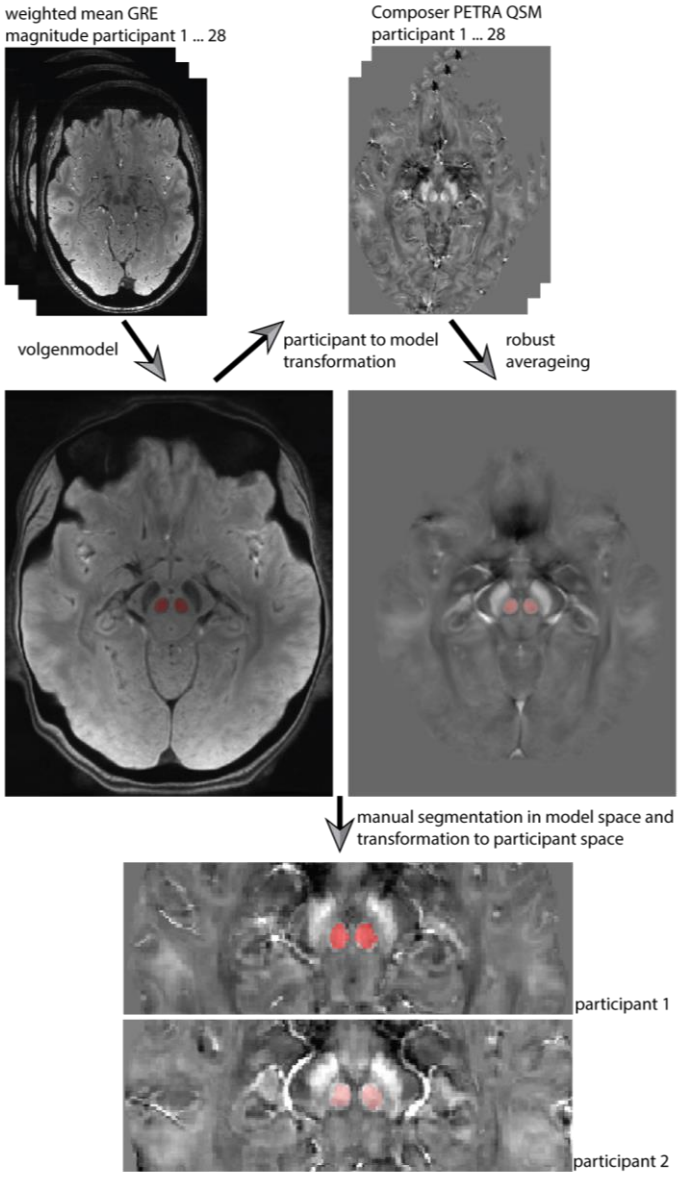


*Figure 2 – Outline of the process associated with atlas based segmentation using volgenmodel. Individual participant data were used to compute a minimum deformation model of the GRE magnitude data. The transformations were then applied to*

*the QSM data. The minimum deformation models were used to segment regions of interest before transforming the segmented region back to subject space.*

# Results

Figure 3 shows the SC susceptibility maps across the top row and the susceptibility maps of the combined phase data in the other rows for an example participant. We compared the different approaches by calculating the absolute difference in susceptibility maps, shown in Figure 4, Figure 5 and Figure 6. The PETRA reference scan and the first echo of the low resolution GRE-MRI (lrGRE1) reconstruction show similar images except for Gibbs ringing artifacts when using the low resolution reference scan, particularly evident in cortical regions (blue arrows in Figure 4). This artefact is due to the fact that only a low spatial resolution image can be obtained using a short echo time GRE-MRI scan. When the second echo of the low resolution GRE-MRI (lrGRE2) reconstruction is used as a reference scan, the first echo combined image has a relatively high noise level due to a very low phase contrast (see Figure 3). Furthermore, these reference scans have a difference in subcortical regions, namely the red nucleus in this particular participant (red arrow, Figure 4). In Figure 4, the comparison between the SC approach and the PETRA reference scan also shows that there is a systematic pattern (green arrows) not apparent in Figure 3.

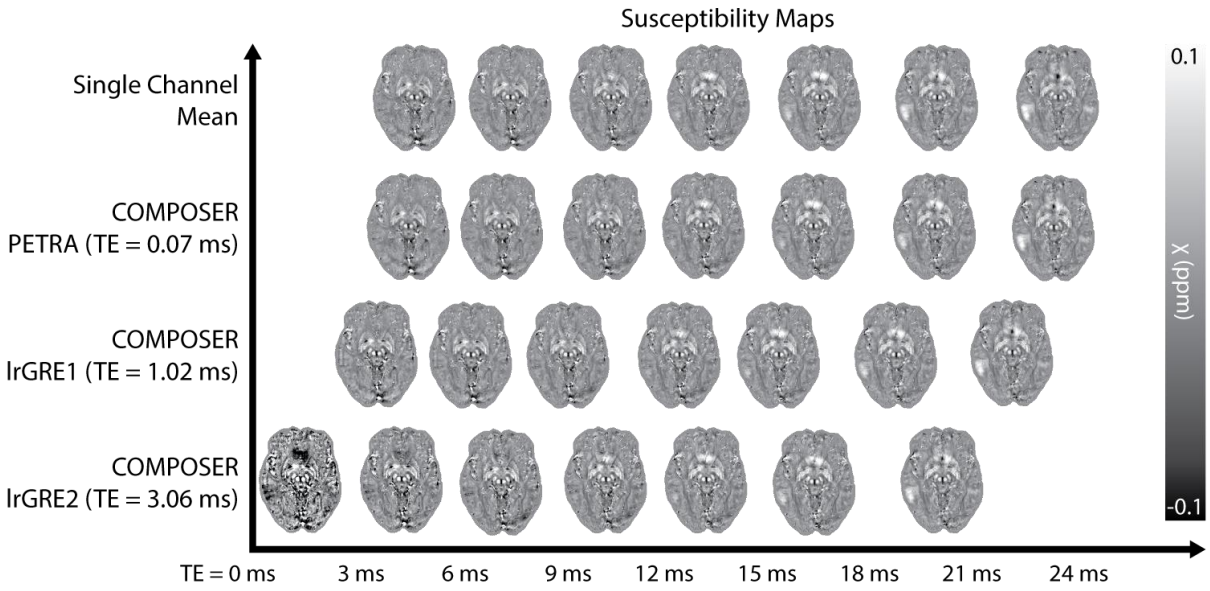


*Figure 3 – Combined susceptibility maps from one representative participant (female, 26 years of age). Displayed are the reference-free single channel method (row 1) and the COMPOSER method (row 2-4) adjusted for the echo time shift introduced by the reference scan. lrGRE – low resolution gradient echo*

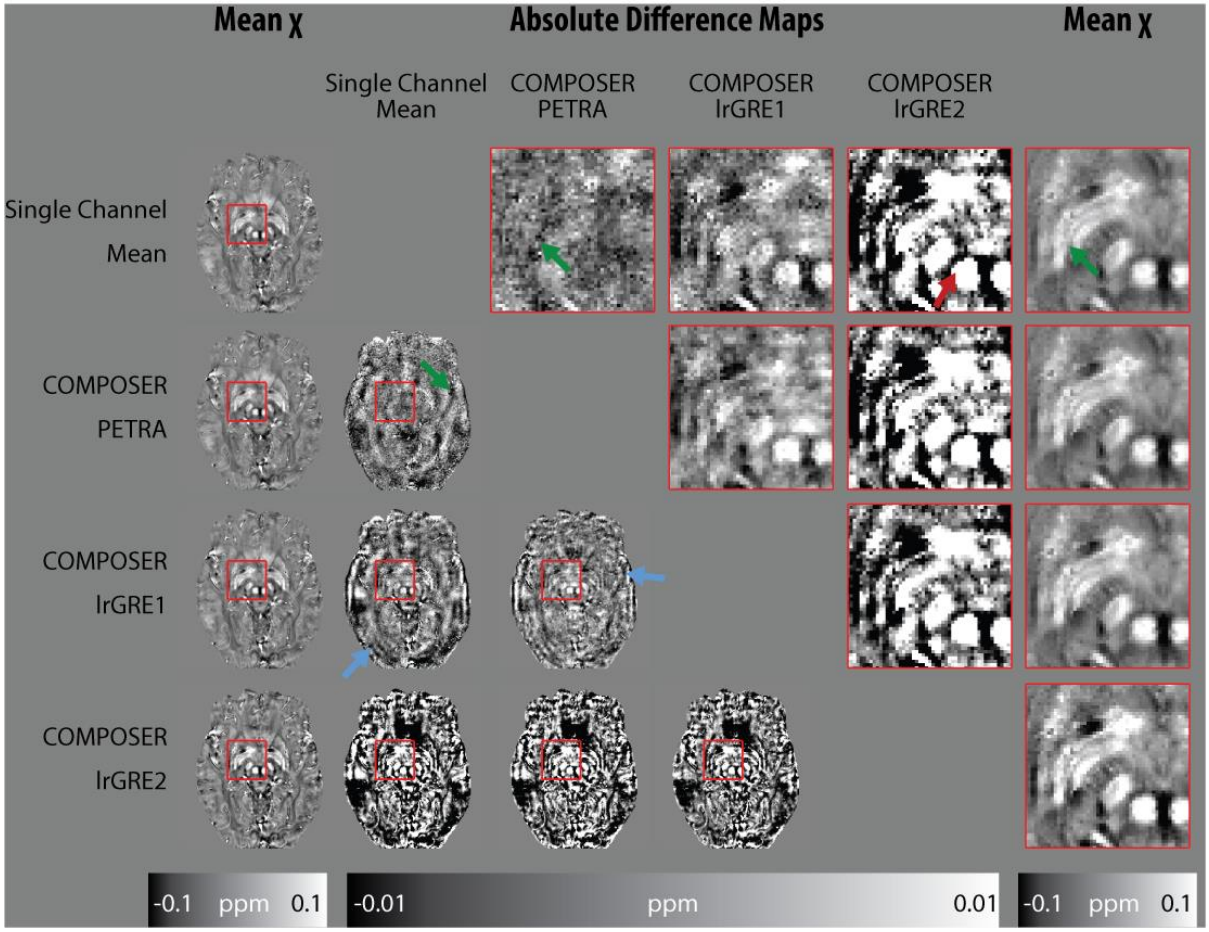


*Figure 4 – Absolute difference maps of all methods in one representative participant (female, 26 years of age) in axial plane. The difference patterns are similar across all subjects studied. The comparison between the single channel approach and the PETRA reference scan shows a structured difference pattern driven by different T2* values of the anatomical structures (green arrows). The low resolution GRE calibration scans introduce ringing artifacts in cortical regions (blue arrows). There is also a difference in subcortical regions like the red nucleus (red arrow) between the different methods. The long TE reference scan shows an altered gray/white matter contrast. lrGRE – low resolution gradient echo.*

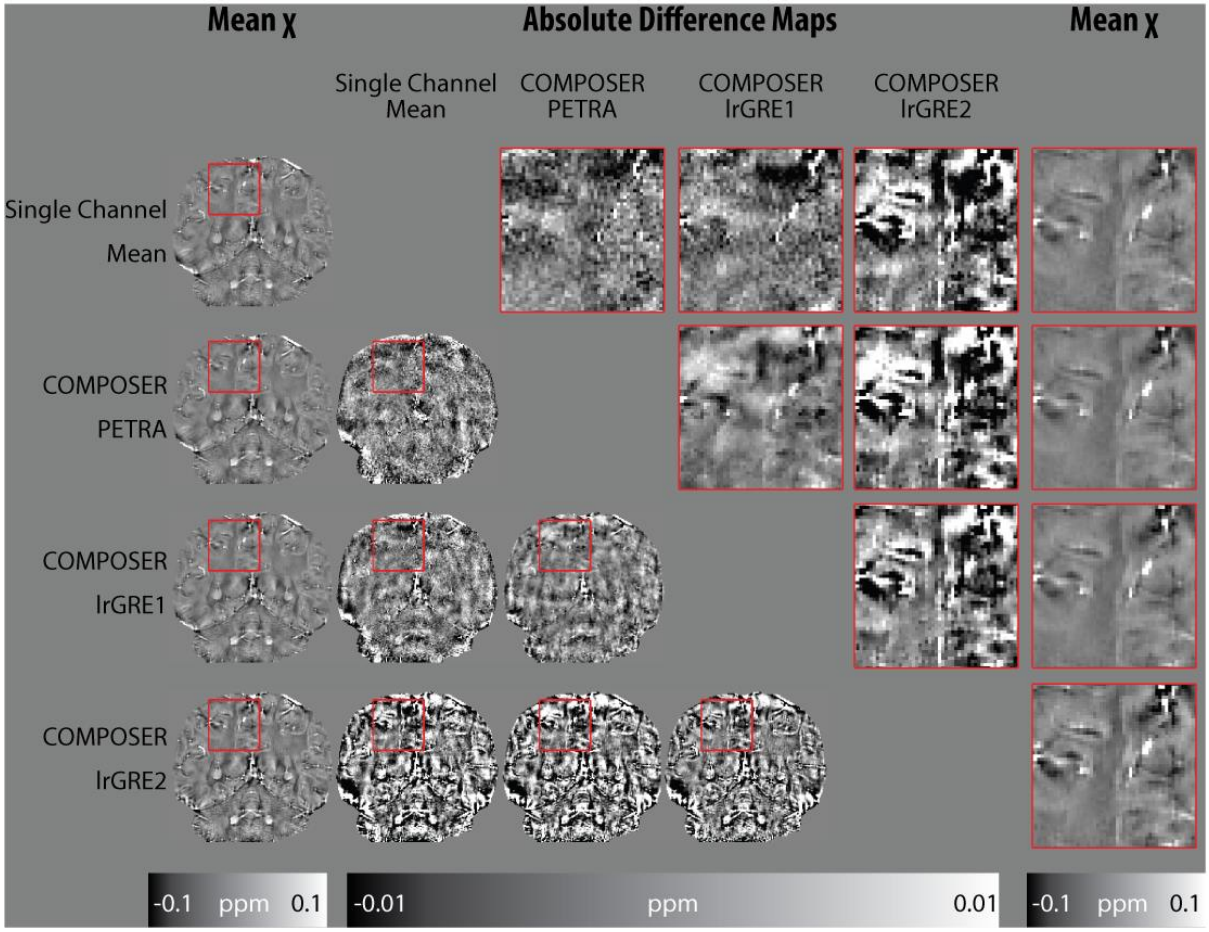


*Figure 5 – Absolute difference maps of all methods in one representative participant (female, 26 years of age) in coronal plane. The difference patterns are similar across all subjects studied. The comparison between the single channel approach and the PETRA reference scan shows a structured difference pattern driven by different T2* values of the anatomical structures. The Gibbs ringing from the low resolution GRE calibration scans is not as visible as in the axial planes. The long TE reference scan shows an altered gray/white matter contrast. lrGRE – low resolution gradient echo.*

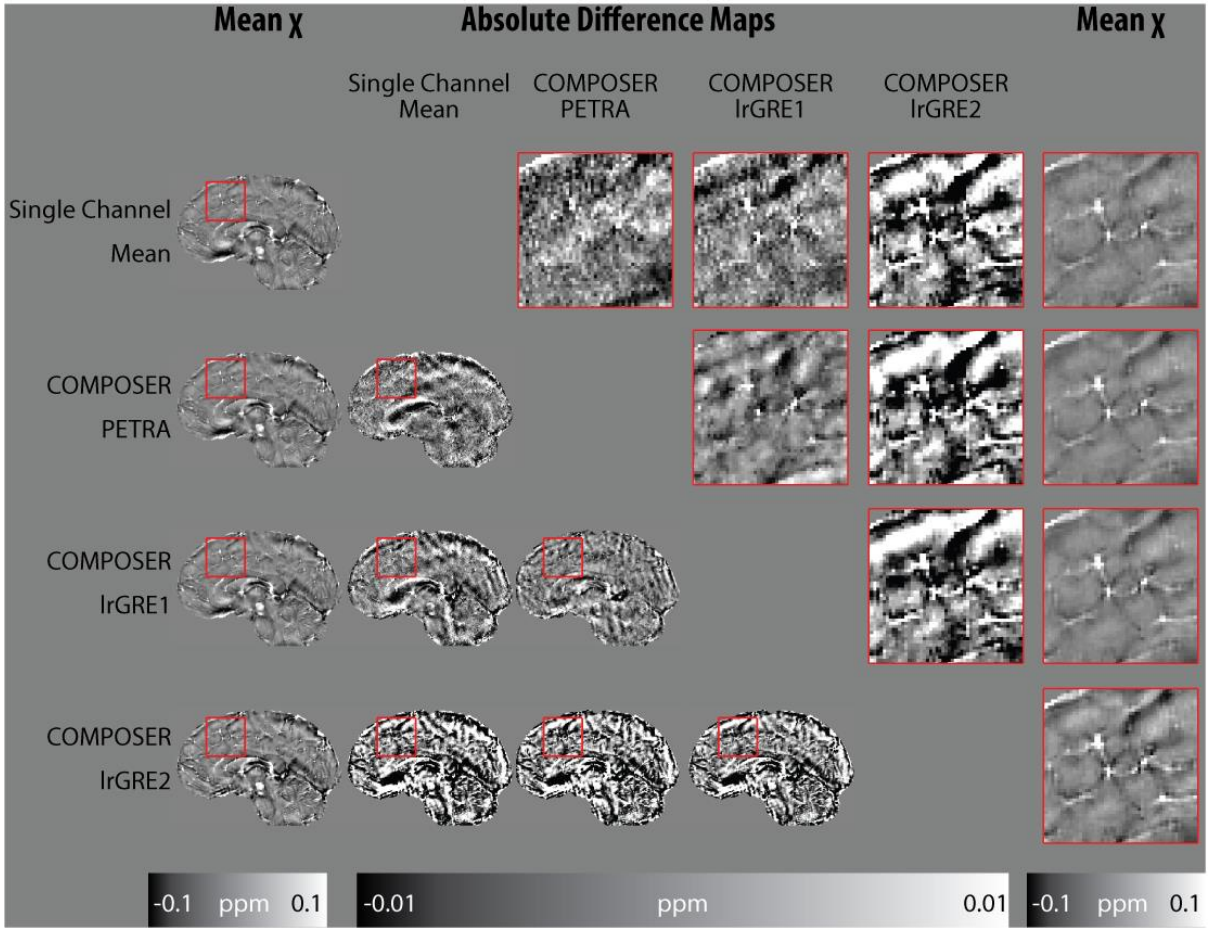


*Figure 6 – Absolute difference maps of all methods in one representative participant (female, 26 years of age) in sagittal plane. The difference patterns are similar across all subjects studied. The comparison between the single channel approach and the PETRA reference scan shows a structured difference pattern driven by different T2* values of the anatomical structures, especially visible in the corpus callosum. The Gibbs ringing from the low resolution GRE calibration scans is not as visible as in the axial planes. The long TE reference scan shows an altered gray/white matter contrast. lrGRE – low resolution gradient echo.*

Assessment of susceptibility values in brain regions considered as a function of echo time are shown in Figure 7. A marked deviation between pipelines exists for early echoes and reduces at later echo times. The relative difference between all COMPOSER combinations and the single channel method is shown in Figure 8. Statistically significant differences ($p < 0.001$, 12 tests, Bonferroni corrected $p < 0.000083$) between single channel method and the COMPOSER combinations have been identified using an asterisk.

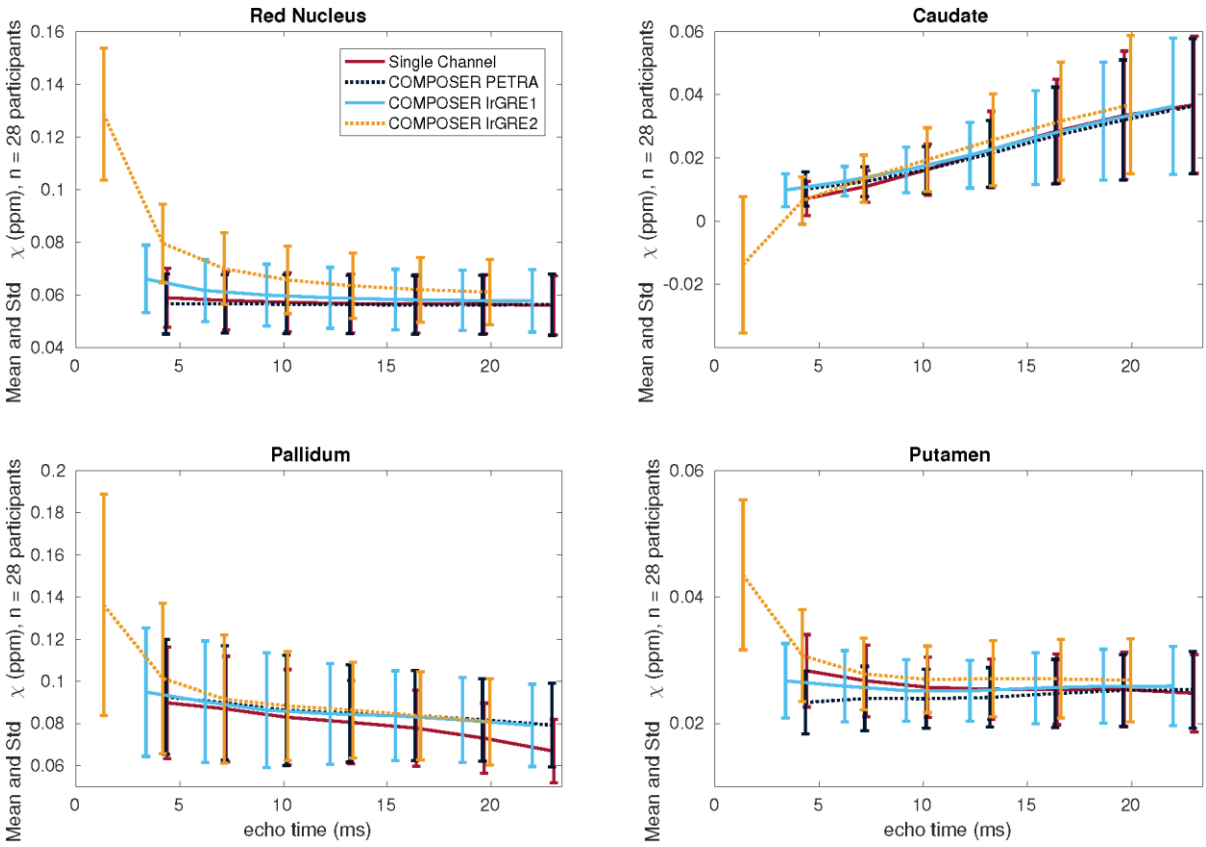


*Figure 7 – Overview of all phase combination approaches versus echo time in all 28 participants. Mean and standard deviation are across subjects. lrGRE – low resolution gradient echo.*

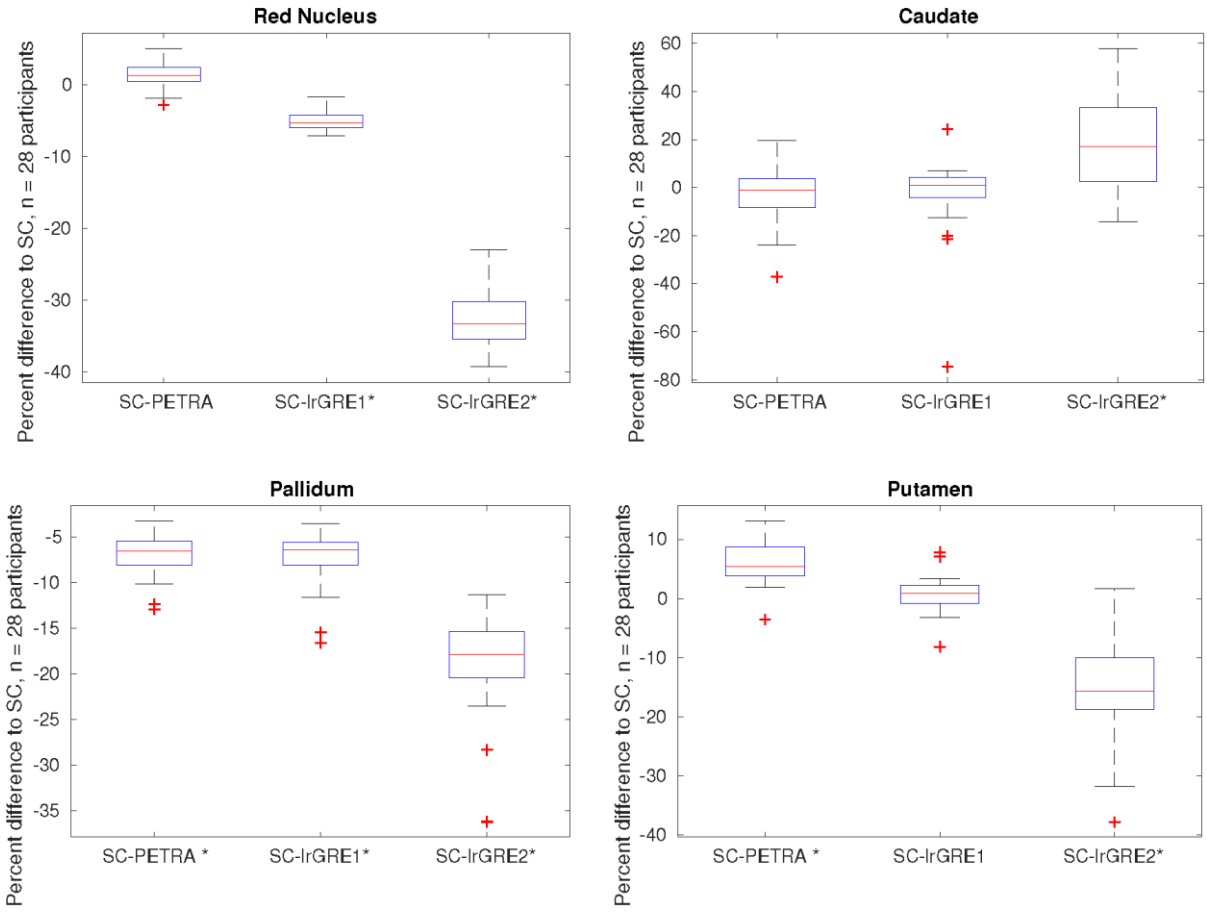


*Figure 8 – Relative difference between COMPOSER combinations and single channel method in percent in all 28 participants averaged across all echo times. SC – single channel, lrGRE – low resolution gradient echo. * indicates significantly different from zero ($p < 0.001$, 12 tests, Bonferroni corrected $p < 0.000083$)*

The 3D EPI channel combination comparison displayed in Figure 9 shows a structural difference in the center of the brain between the two combination methods chosen. The Gibbs ringing artifacts of the low resolution GRE-MRI reconstruction are not as clearly visible as in the GRE-MRI combination.

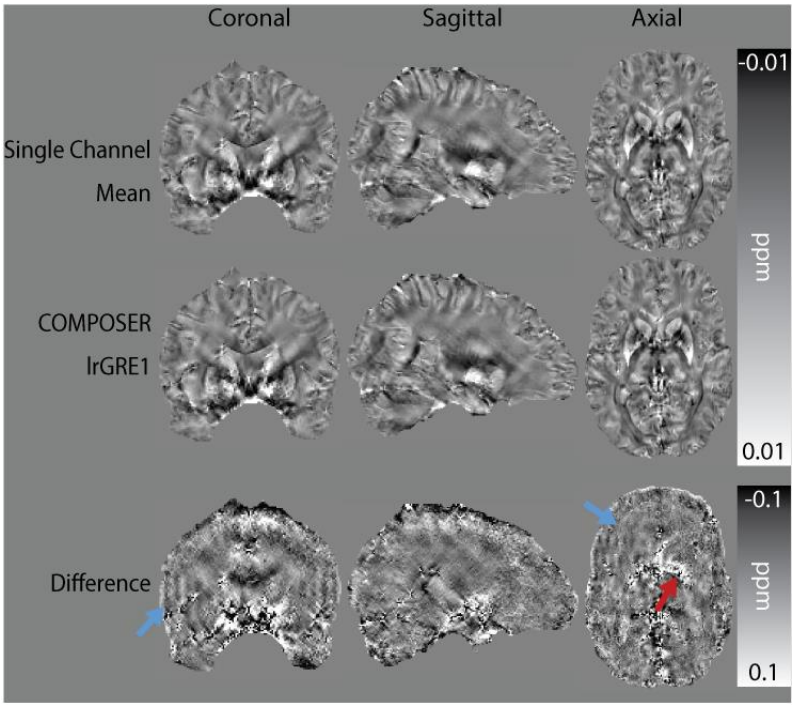


*Figure 9 – 3D EPI based QSM reconstructions and difference maps in one example participant (male, 44 years of age). Both COMPOSER and SC deliver artifact free susceptibility maps for 3D EPI data. The Gibbs ringing artifacts of the low resolution GRE reference are visible in cortical regions (blue arrows). There is a structural difference between the two combination methods in the center of the brain (red arrow). lrGRE – low resolution gradient echo.*

## Discussion

We investigated the impact of the choice of coil combination method on QSM results at 7 T and studied how the quality and echo time of the reference scan affects quantitation following a COMPOSER coil combination. We explored how an alternative method, where the phase data is not combined before the QSM pipeline, but processed channel-by-channel, compares to the COMPOSER phase combination approach. Additionally, we explored the application of the COMPOSER method and the single channel approach to 3D EPI data.

By comparing various approaches for combining individual channel data in relation to QSM, we found that susceptibility results are influenced by the method used to combine MRI phase data. The quality of the result obtained using the COMPOSER method can be affected by two main factors: the echo time of the reference scan; and, artifacts in the reference scan. The reference scan should have an echo time as short as possible to not introduce artificial phase contrast and quantitation bias. We found that even short echo time reference scans (i.e. 1 ms) introduce a bias in the quantitation at 7 T, and ultra-short TE reference scans can reduce this bias.

The Gibbs ringing artifacts in the low resolution reference scans can be avoided by opting for a higher resolution alternative if an ultra-short echo time reference scan is not available. It might also be possible to reduce the Gibbs ringing artifacts in a post processing step by interpolating, normalizing and smoothing the complex data using a polynomial fitting procedure as in the SENSE reconstruction (38).

The single channel method delivered comparable quantitation results to COMPOSER with PETRA and COMPOSER with lrGRE1 without suffering from combination artifacts, as seen with the low resolution GRE reference scans. This is interesting as one could expect that the residual contributions from transmit and receive phase affect the quantitation, but these contributions appear to have fairly low spatial frequencies and have been removed during the background field correction in TGV. In the supporting material we show that not all background field corrections can suppress B1 contributions (Supporting Figure S1 and S2). When using vSHARP, which assumes harmonic background fields, it can be seen that residual B1 components cannot be suppressed fully as already demonstrated by Schweser and colleagues (51).

The single channel method does require a larger amount of data storage and processing resources, but can be a feasible and fast option with the use of multi-core computing environments. On a workstation with an Intel Xeon CPU E5-2695 v3 @ 2.30GHz it takes 3 minutes to process a single channel using TGV and in total 32 channels and 7 echoes sum to about 11 hours per participant. If there is no cluster available one could apply channel compression techniques (29,52) to reduce the amount of processing required.

The idea to combine phase data after certain processing steps has been pointed out by others as well, where it was shown that the channel-by-channel processing of phase data delivers better results than with standard pipelines in susceptibility weighted imaging (SWI) (53). The single channel method can be improved further by building masks per channel and excluding low magnitude signal regions from the QSM pipeline, as performed in (54), or only selecting channels with a high phase quality (55).

Based on our results we identified two methods of choice depending on priorities: 1) The additional two minute PETRA reference scan offers high quality phase combination, allows the removal of transmit phase effects, and can be applied to single echo acquisitions. The PETRA acquisition can potentially be shortened to 35 seconds by reducing the amount of acquired spokes as illustrated in the supporting material 2) If such a reference scan is not available, the single channel method delivers similar results in the brain regions considered here. We also found that both methods can be applied to successfully process single echo 3D EPI data.

We have not tested the influence of different coil combination methods on bipolar acquisitions, which have been used to increase the number of echo times set in the acquisition, improve unwrapping and compensate for laminar flow effects (56). Bipolar readouts utilize positive and negative readout gradients and lead to different eddy current and readout gradient phase effects. Although odd and even echoes would have different phase offsets, the methods tested here should be robust to such effects as our evaluation was not based on multiple echo time data. However, if the reference scan has the same readout direction as the odd echoes, it will only remove the phase gradient in the odd echoes. The reference scan will introduce an additional phase gradient in the even echoes (39).

In conclusion, our comparison of the various approaches shows that reference scans can bias QSM results. An ultra-short echo time reference scan reduces this bias and performing QSM channel-by-channel leads to consistent results and provides a robust method that worked for all tested sequences, including echo planar imaging. Channel combination in the single channel QSM approach is not performed as a first step, instead the QSM pipeline is applied to each channel and a combined result is obtained as the last step without the need for an additional reference scan. This allows for the application of the single channel method to a very broad range of acquisition schemes, including single-echo acquisition schemes and situations where a volume reference coil is not available.

# References


1. Duyn J. MR susceptibility imaging. J. Magn. Reson. 2013;229:198–207. doi: 10.1016/j.jmr.2012.11.013.

2. Reichenbach JR. The future of susceptibility contrast for assessment of anatomy and function. NeuroImage 2012;62:1311–1315. doi: 10.1016/j.neuroimage.2012.01.004.

3. Schweser F, Deistung A, Reichenbach JR. Foundations of MRI phase imaging and processing for Quantitative Susceptibility Mapping (QSM). Z. Für Med. Phys. [Internet] 2015. doi: 10.1016/j.zemedi.2015.10.002.

4. Wang Y, Liu T. Quantitative susceptibility mapping (QSM): Decoding MRI data for a tissue magnetic biomarker. Magn. Reson. Med. 2015;73:82–101. doi: 10.1002/mrm.25358.

5. Shmueli K, de Zwart JA, van Gelderen P, Li T-Q, Dodd SJ, Duyn JH. Magnetic susceptibility mapping of brain tissue in vivo using MRI phase data. Magn. Reson. Med. 2009;62:1510–1522. doi: 10.1002/mrm.22135.

6. Langkammer C, Liu T, Khalil M, Enzinger C, Jehna M, Fuchs S, Fazekas F, Wang Y, Ropele S. Quantitative Susceptibility Mapping in Multiple Sclerosis. Radiology 2013;267:551–559. doi: 10.1148/radiol.12120707.

7. Langkammer C, Schweser F, Krebs N, et al. Quantitative susceptibility mapping (QSM) as a means to measure brain iron? A post mortem validation study. NeuroImage 2012;62:1593–1599. doi: 10.1016/j.neuroimage.2012.05.049.

8. Liu T, Surapaneni K, Lou M, Cheng L, Spincemaille P, Wang Y. Cerebral microbleeds: burden assessment by using quantitative susceptibility mapping. Radiology 2012;262:269–278.

9. Schweser F, Deistung A, Lehr BW, Reichenbach JR. Differentiation between diamagnetic and paramagnetic cerebral lesions based on magnetic susceptibility mapping. Med. Phys. 2010;37:5165. doi: 10.1118/1.3481505.

10. Acosta-Cabronero J, Betts MJ, Cardenas-Blanco A, Yang S, Nestor PJ. In Vivo MRI Mapping of Brain Iron Deposition across the Adult Lifespan. J. Neurosci. 2016;36:364–374. doi: 10.1523/JNEUROSCI.1907-15.2016.

11. Bilgic B, Pfefferbaum A, Rohlfing T, Sullivan EV, Adalsteinsson E. MRI estimates of brain iron concentration in normal aging using quantitative susceptibility mapping. NeuroImage 2012;59:2625–2635. doi: 10.1016/j.neuroimage.2011.08.077.

12. Bergen JMG van, Hua J, Unschuld PG, Lim I a. L, Jones CK, Margolis RL, Ross CA, Zijl PCM van, Li X. Quantitative Susceptibility Mapping Suggests Altered Brain Iron in Premanifest Huntington Disease. Am. J. Neuroradiol. [Internet] 2015. doi: 10.3174/ajnr.A4617.

13. Eskreis-Winkler S, Deh K, Gupta A, Liu T, Wisnieff C, Jin M, Gauthier SA, Wang Y, Spincemaille P. Multiple sclerosis lesion geometry in quantitative susceptibility mapping (QSM) and phase imaging. J. Magn. Reson. Imaging 2014:n/a-n/a. doi: 10.1002/jmri.24745.

14. Stüber C, Pitt D, Wang Y. Iron in Multiple Sclerosis and Its Noninvasive Imaging with Quantitative Susceptibility Mapping. Int. J. Mol. Sci. 2016;17:100. doi: 10.3390/ijms17010100.

15. Acosta-Cabronero J, Williams GB, Cardenas-Blanco A, Arnold RJ, Lupson V, Nestor PJ. In Vivo Quantitative Susceptibility Mapping (QSM) in Alzheimer's Disease. PLoS ONE 2013;8:e81093. doi: 10.1371/journal.pone.0081093.

16. Lotfipour AK, Wharton S, Schwarz ST, Gontu V, Schäfer A, Peters AM, Bowtell RW, Auer DP, Gowland PA, Bajaj NPS. High resolution magnetic susceptibility mapping of the substantia nigra in Parkinson's disease. J. Magn. Reson. Imaging 2012;35:48–55. doi: 10.1002/jmri.22752.

17. Murakami Y, Kakeda S, Watanabe K, et al. Usefulness of Quantitative Susceptibility Mapping for the Diagnosis of Parkinson Disease. Am. J. Neuroradiol. [Internet] 2015. doi: 10.3174/ajnr.A4260.

18. de Hollander G, Keuken MC, Bazin P-L, Weiss M, Neumann J, Reimann K, Wähnert M, Turner R, Forstmann BU, Schäfer A. A gradual increase of iron toward the medial-inferior tip of the subthalamic nucleus: A Medial-Inferior Iron Gradient in the STN. Hum. Brain Mapp. 2014;35:4440–4449. doi: 10.1002/hbm.22485.

19. Lupo JM, Essock-Burns E, Molinaro AM, Cha S, Chang SM, Butowski N, Nelson SJ. Using susceptibility-weighted imaging to determine response to combined anti-angiogenic, cytotoxic, and radiation therapy in patients with glioblastoma multiforme. Neuro-Oncol. 2013;15:480–489. doi: 10.1093/neuonc/nos325.

20. Theysohn JM, Kraff O, Maderwald S, Barth M, Ladd SC, Forsting M, Ladd ME, Gizewski ER. 7 tesla MRI of microbleeds and white matter lesions as seen in vascular dementia. J. Magn. Reson. Imaging 2011;33:782–791. doi: 10.1002/jmri.22513.

21. Ge Y, Zohrabian VM, Grossman RI. Seven-Tesla Magnetic Resonance Imaging: New Vision of Microvascular Abnormalities in Multiple Sclerosis. Arch. Neurol. [Internet] 2008;65. doi: 10.1001/archneur.65.6.812.

22. McVeigh ER, Bronskill MJ, Henkelman RM. Phase and sensitivity of receiver coils in magnetic resonance imaging. Med. Phys. 1986;13:806–814.

23. Robinson SD, Bredies K, Khabipova D, Dymerska B, Marques JP, Schweser F. An illustrated comparison of processing methods for MR phase imaging and QSM: combining array coil signals and phase unwrapping. NMR Biomed. 2016:n/a-n/a. doi: 10.1002/nbm.3601.

24. Strasser B, Chmelik M, Robinson SD, Hangel G, Gruber S, Trattnig S, Bogner W. Coil combination of multichannel MRSI data at 7 T: MUSICAL. NMR Biomed. 2013;26:1796–1805. doi: 10.1002/nbm.3019.

25. Noll DC, Nishimura DG, Macovski A. Homodyne detection in magnetic resonance imaging. IEEE Trans. Med. Imaging 1991;10:154–163. doi: 10.1109/42.79473.

26. Koopmans PJ, Manniesing R, Niessen WJ, Viergever MA, Barth M. MR venography of the human brain using susceptibility weighted imaging at very high field strength. Magn. Reson. Mater. Phys. Biol. Med. 2008;21:149–158. doi: 10.1007/s10334-007-0101-3.

27. Rauscher A, Barth M, Reichenbach JR, Stollberger R, Moser E. Automated unwrapping of MR phase images applied to BOLD MR-venography at 3 Tesla. J. Magn. Reson. Imaging 2003;18:175–180. doi: 10.1002/jmri.10346.

28. Buehrer M, Boesiger P, Kozerke S. Virtual body coil calibration for phased-array imaging. In: ISMRM 17th Scientific Meetings. ; 2009.

29. Buehrer M, Pruessmann KP, Boesiger P, Kozerke S. Array compression for MRI with large coil arrays. Magn. Reson. Med. 2007;57:1131–1139. doi: 10.1002/mrm.21237.

30. Hammond KE, Lupo JM, Xu D, Metcalf M, Kelley DAC, Pelletier D, Chang SM, Mukherjee P, Vigneron DB, Nelson SJ. Development of a robust method for generating 7.0 T multichannel phase images of the brain with application to normal volunteers and patients with neurological diseases. NeuroImage 2008;39:1682–1692. doi: 10.1016/j.neuroimage.2007.10.037.

31. Parker DL, Payne A, Todd N, Hadley JR. Phase reconstruction from multiple coil data using a virtual reference coil. Magn. Reson. Med. 2014;72:563–569. doi: 10.1002/mrm.24932.

32. Lu K, Liu TT, Bydder M. Optimal phase difference reconstruction: comparison of two methods. Magn. Reson. Imaging 2008;26:142–145. doi: 10.1016/j.mri.2007.04.015.

33. Thunberg P, Karlsson M, Wigström L. Comparison of different methods for combining phase-contrast images obtained with multiple coils. Magn. Reson. Imaging 2005;23:795–799. doi: 10.1016/j.mri.2005.06.002.

34. Bernstein MA, Grgic M, Brosnan TJ, Pelc NJ. Reconstructions of phase contrast, phased array multicoil data. Magn. Reson. Med. 1994;32:330–334.

35. Robinson S, Grabner G, Witoszynskyj S, Trattnig S. Combining phase images from multi-channel RF coils using 3D phase offset maps derived from a dual-echo scan. Magn. Reson. Med. 2011;65:1638–1648. doi: 10.1002/mrm.22753.

36. Dagher J, Nael K. MAGPI: A framework for maximum likelihood MR phase imaging using multiple receive coils. Magn. Reson. Med. 2016;75:1218–1231. doi: 10.1002/mrm.25756.

37. Khabipova D, Wiaux Y, Gruetter R, Marques JP. A modulated closed form solution for quantitative susceptibility mapping — A thorough evaluation and comparison to iterative methods based on edge prior knowledge. NeuroImage 2015;107:163–174. doi: 10.1016/j.neuroimage.2014.11.038.

38. Pruessmann KP, Weiger M, Scheidegger MB, Boesiger P. SENSE: sensitivity encoding for fast MRI. Magn. Reson. Med. Off. J. Soc. Magn. Reson. Med. Soc. Magn. Reson. Med. 1999;42:952–962.

39. Robinson SD, Dymerska B, Bogner W, Barth M, Zaric O, Goluch S, Grabner G, Deligianni X, Bieri O, Trattnig S. Combining phase images from array coils using a short echo time reference scan (COMPOSER). Magn. Reson. Med. 2015:n/a-n/a. doi: 10.1002/mrm.26093.

40. Bollmann S, Zimmer F, O'Brien K, Vegh V, Barth M. When to Perform Channel Combination in 7 Tesla Quantitative Susceptibility Mapping? In: Proceedings of the 21st Annual Meeting of the Organization for Human Brain Mapping. Honolulu; 2015.

41. Robinson S, Schödl H, Trattnig S. A method for unwrapping highly wrapped multi-echo phase images at very high field: UMPIRE: UMPIRE-Unwrapping Multi-echo Phase Images. Magn. Reson. Med. 2014;72:80–92. doi: 10.1002/mrm.24897.

42. Grodzki DM, Jakob PM, Heismann B. Ultrashort echo time imaging using pointwise encoding time reduction with radial acquisition (PETRA). Magn. Reson. Med. 2012;67:510–518. doi: 10.1002/mrm.23017.

43. Jenkinson M, Bannister P, Brady M, Smith S. Improved optimization for the robust and accurate linear registration and motion correction of brain images. NeuroImage 2002;17:825–841.

44. Jenkinson M, Smith S. A global optimisation method for robust affine registration of brain images. Med. Image Anal. 2001;5:143–156.

45. Langkammer C, Bredies K, Poser BA, Barth M, Reishofer G, Fan AP, Bilgic B, Fazekas F, Mainero C, Ropele S. Fast quantitative susceptibility mapping using 3D EPI and total generalized variation. NeuroImage 2015;111:622–630. doi: 10.1016/j.neuroimage.2015.02.041.

46. Smith SM. Fast robust automated brain extraction. Hum. Brain Mapp. 2002;17:143–155. doi: 10.1002/hbm.10062.

47. Grabner G, Janke AL, Budge MM, Smith D, Pruessner J, Collins DL. Symmetric atlasing and model based segmentation: an application to the hippocampus in older adults. In: Medical Image Computing and Computer-Assisted Intervention–MICCAI 2006. Springer; 2006. pp. 58–66.

48. Fonov V, Evans AC, Botteron K, Almli CR, McKinstry RC, Collins DL. Unbiased average age-appropriate atlases for pediatric studies. NeuroImage 2011;54:313–327. doi: 10.1016/j.neuroimage.2010.07.033.

49. Janke AL, Ullmann JFP. Robust methods to create ex vivo minimum deformation atlases for brain mapping. Methods 2015;73:18–26. doi: 10.1016/j.ymeth.2015.01.005.

50. Yushkevich PA, Piven J, Hazlett HC, Smith RG, Ho S, Gee JC, Gerig G. User-guided 3D active contour segmentation of anatomical structures: significantly improved efficiency and reliability. NeuroImage 2006;31:1116–1128. doi: 10.1016/j.neuroimage.2006.01.015.

51. Schweser F, Atterbury M, Deistung A, Lehr BW, Sommer K, Reichenbach JR. Harmonic phase subtraction methods are prone to B1 background components. In: Proc ISMRM. Vol. 19. ; 2011. p. 2657.

52. Zhang T, Pauly JM, Vasanawala SS, Lustig M. Coil Compression for Accelerated Imaging with Cartesian Sampling. Magn. Reson. Med. Off. J. Soc. Magn. Reson. Med. Soc. Magn. Reson. Med. 2013;69:571–582. doi: 10.1002/mrm.24267.

53. Hosseini Z, Liu J, Solovey I, Menon RS, Drangova M. Susceptibility-weighted imaging using inter-echo-variance channel combination for improved contrast at 7 tesla. J. Magn. Reson. Imaging 2016:n/a-n/a. doi: 10.1002/jmri.25409.

54. Sood S, Urriola J, Reutens D, O'Brien K, Bollmann S, Barth M, Vegh V. Echo time-dependent quantitative susceptibility mapping contains information on tissue properties. Magn. Reson. Med. 2016:n/a-n/a. doi: 10.1002/mrm.26281.

55. Vegh V, O'Brien K, Barth M, Reutens DC. Selective channel combination of MRI signal phase. Magn. Reson. Med. 2015:n/a-n/a. doi: 10.1002/mrm.26057.

56. Feng W, Neelavalli J, Haacke EM. Catalytic multiecho phase unwrapping scheme (CAMPUS) in multiecho gradient echo imaging: removing phase wraps on a voxel-by-voxel basis. Magn. Reson. Med. 2013;70:117–126. doi: 10.1002/mrm.24457.

# Supporting Material

We have acquired additional data in one participant (female, 24 years of age) to compare the ROEMER volume coil reference approach to the methods discussed in the manuscript and to show the impact of reducing the acquisition time for the PETRA reference scan.

For the ROEMER approach we acquired two 3D GRE with 3 echoes using first the 32 array elements and in the second acquisition the volume coil with the following parameters: TR = 8 ms, TE = 1.02, 3.06, 6.12 ms, flip angle = 5°, FOV = 245x245x182 mm3, matrix = 70x70x52 (3.5 mm isometric voxels), monopolar readout gradient, symmetric echo, 1211 Hz/Pixel, TA = 24 s.

It is also possible to reduce the acquisition time of the PETRA scan from 120 seconds to 35 seconds by reducing the amount of spokes. To provide an example we acquired an additional PETRA dataset with the following parameters: TR = 1.99 ms, TE = 0.07 ms, flip angle = 2°, FOV = 288x288x288 $mm^3$, matrix = 288x288x288 (1 mm isometric voxels), 847 Hz/Pixel, TA = 35 s and reduced the amount of acquired spokes by a factor of 5 from 50 000 to 10 000. This is an undersampled acquisition with limited artifacts.

The PETRAfast acquisition delivers similar results to the high quality scan, but shows some ringing artifacts as illustrated in Supporting Figure S1.

To illustrate the influence of the employed background field correction, we first processed the data identically to the manuscript with the TGV pipeline:

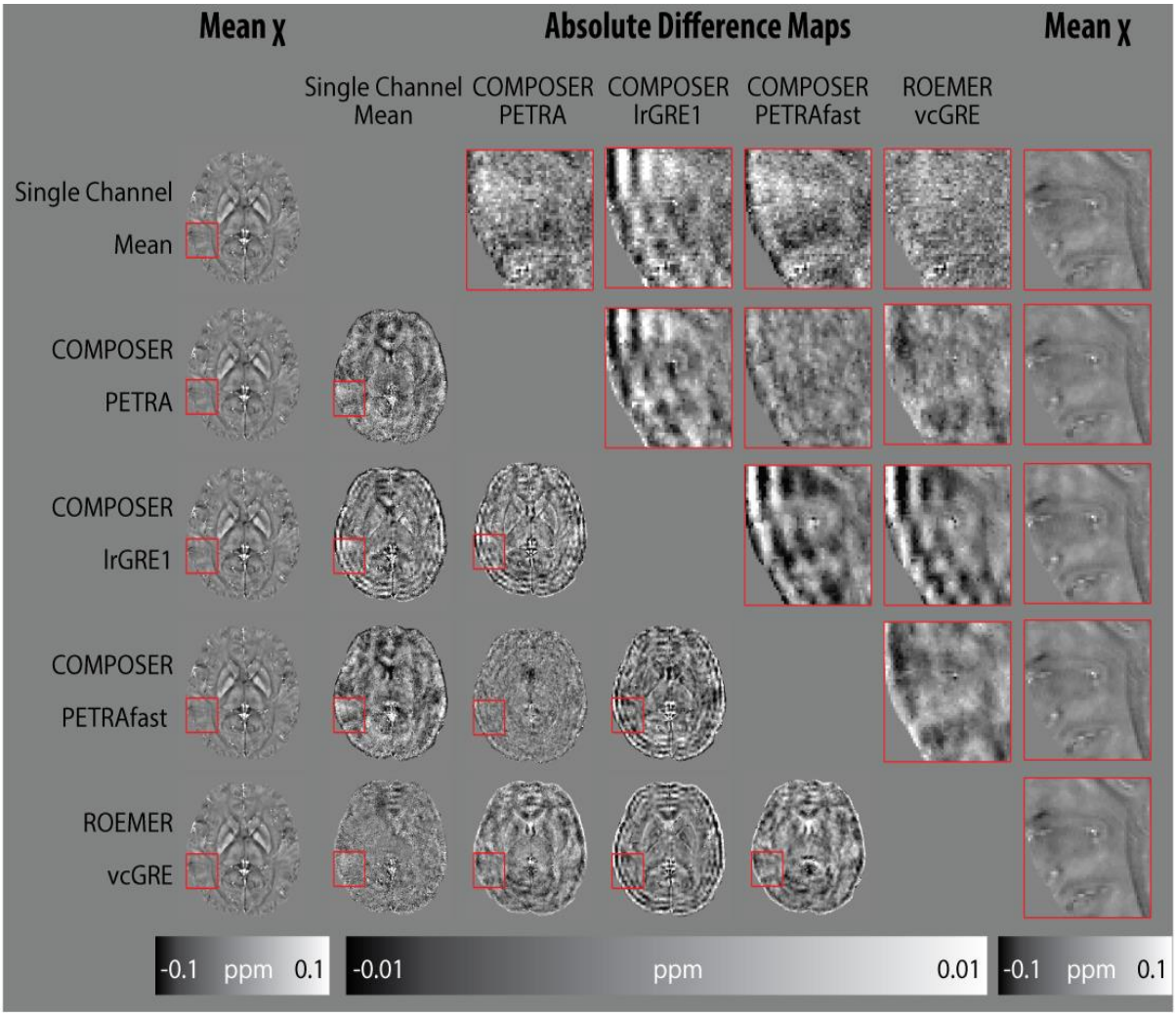


*Supporting Figure S1 - Absolute difference maps in one additionally acquired participant (female, 24 years of age) processed using TGV. The comparison between the single channel approach and the PETRA reference scan shows a structured difference pattern driven by different T2* values of the anatomical structures. The low resolution GRE calibration scan introduces ringing artifacts in cortical regions. The PETRAfast calibration scan shows similar results to the normal PETRA acquisition but ringing artifacts become observable. The ROEMER approach delivers similar results to the single channel method and does not show any obvious artifacts except for Gibbs ringing. lrGRE – low resolution gradient echo, vcGRE – volume coil gradient echo.*

In this single subject dataset, we can see that the volume coil-based reconstruction (ROEMER vcGRE) delivers an artifact free susceptibility map. A slight disadvantage of the ROEMER approach are the Gibbs ringing artifacts visible by comparing the single channel method and the Roemer approach. The comparison with e.g. COMPOSER with a PETRA reference scan shows that the arbitrary phase components from the inhomogeneous reference coil are largely removed by the regularized background field correction in TGV.

This is not true for all background subtraction methods, however. Schweser at al. (1) have shown that harmonic component subtraction methods such as PDF and SHARP cannot eliminate B1+ at ultra-high field. This can be seen when we use vSHARP (and iLSQR as inversion) as implemented in STISuite (2) to reconstruct the Susceptibility maps in Supporting Figure S2:

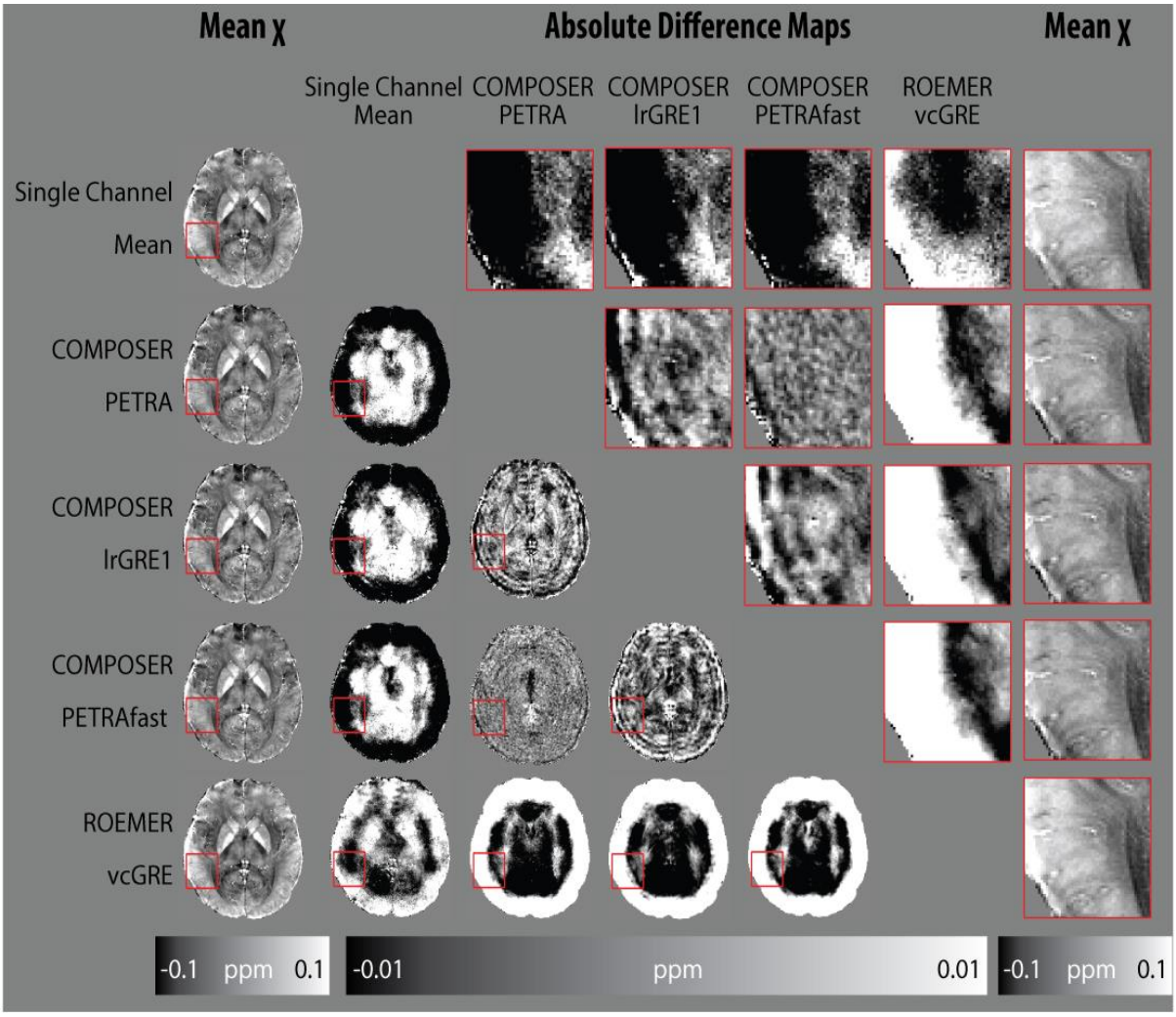


*Supporting Figure S2 - Absolute difference maps in one additionally acquired participant (female, 24 years of age) processed using vSHARP and iLSQR. vSHARP is not able to remove the residual B1 components in the ROEMER and single channel approach, whereas the COMPOSER based reconstructions do not show this problem. lrGRE – low resolution gradient echo, vcGRE – volume coil gradient echo.*

When using vSHARP as a background field correction we can see that the ROEMER and the single channel approach have a considerable residual background field due to B1+ components which are not removed by the background field correction.

It can be shown that the Roemer combined target scan contains the transmit and receive phase from the volume coil (VC):

The complex image data S from the coils to be combined is given by:

$$\boldsymbol{S}_{TAR,RC} = \boldsymbol{M}_{TAR,RC} \cdot e^{i\left(2\pi\Delta B_0 TE_{TAR} + k\left(B_{1\,VC}^{+} + \boldsymbol{B}_{1\,RC}^{-}\right)\right)} \qquad [1]$$

VC – volume coil, transmit coil

RC – Receive coils

K – constant converting B1 field to a phase

The complex image data of the reference scan using the volume coil is:

$$S_{REF,VC} = M_{REF,VC} \cdot e^{i\left(2\pi\Delta B_0 TE_{REF} + k\left(B_1^+{}_{VC} + B_1^-{}_{VC}\right)\right)} \quad [2]$$

The complex image data of the reference scan using the receive coils is:

$$\boldsymbol{S}_{REF,RC} = \boldsymbol{M}_{REF,RC} \cdot e^{i\left(2\pi\Delta B_0 TE_{REF} + k\left(B_1^+{}_{VC} + \boldsymbol{B}_1^-{}_{RC}\right)\right)} \quad [3]$$

The coil sensitivities are the ratio of the signals from the reference scans (i.e. [2]/[3]):

$$\boldsymbol{R} = \left(\frac{M_{REF,VC}}{\boldsymbol{M}_{REF,RC}}\right) \cdot e^{i\left(k\left(B_1^-{}_{VC} - \boldsymbol{B}_1^-{}_{RC}\right)\right)} \quad [4]$$

The combined signal from the receive coils (RC) of the target scan is the product of [1] and [4]:

$$\boldsymbol{S}_{TAR,RC} = \boldsymbol{M}_{TAR,RC} \cdot e^{i\left(2\pi\Delta B_0 TE_{TAR} + k\left(B_1^+{}_{VC} + \boldsymbol{B}_1^-{}_{RC}\right)\right)} \cdot \left(\frac{M_{REF,VC}}{\boldsymbol{M}_{REF,RC}}\right) \cdot e^{i\left(k\left(B_1^-{}_{VC} - \boldsymbol{B}_1^-{}_{RC}\right)\right)}$$

$$\boldsymbol{S}_{TAR,RC} = \left(\frac{\boldsymbol{M}_{TAR,RC} \cdot M_{REF,VC}}{\boldsymbol{M}_{REF,RC}}\right) \cdot e^{i\left(2\pi\Delta B_0 TE_{TAR} + k\left(B_1^+{}_{VC} + \boldsymbol{B}_1^-{}_{RC}\right) + k\left(B_1^-{}_{VC} - \boldsymbol{B}_1^-{}_{RC}\right)\right)}$$

$$\boldsymbol{S}_{TAR,RC} = \left(\frac{\boldsymbol{M}_{TAR,RC} \cdot M_{REF,VC}}{\boldsymbol{M}_{REF,RC}}\right) \cdot e^{i\left(2\pi\Delta B_0 TE_{TAR} + k\left(B_1^+{}_{VC} + \boldsymbol{B}_1^-{}_{RC} + B_1^-{}_{VC} - B_1^-{}_{RC}\right)\right)}$$

$$\boldsymbol{S}_{TAR,RC} = \left(\frac{\boldsymbol{M}_{TAR,RC} \cdot M_{REF,VC}}{\boldsymbol{M}_{REF,RC}}\right) \cdot e^{i\left(2\pi\Delta B_0 TE_{TAR} + k\left(B_1^+{}_{VC} + B_1^-{}_{VC}\right)\right)}$$

This shows that the Roemer combined target scan contains the transmit and receive phase from the transmit Coil VC.

# References


1. Schweser F, Atterbury M, Deistung A, Lehr BW, Sommer K, Reichenbach JR. Harmonic phase subtraction methods are prone to B1 background components. In: Proc ISMRM. Vol. 19. ; 2011. p. 2657.

2. Li W, Avram AV, Wu B, Xiao X, Liu C. Integrated Laplacian-based phase unwrapping and background phase removal for quantitative susceptibility mapping. NMR Biomed. 2014;27:219–227. doi: 10.1002/nbm.3056.